Multiparametric MRI and imaging transcriptomics reveal molecular and cellular correlates of neurodegeneration in experimental multiple system atrophy

Eugene Kim[1], Diana Cash[1], Daniel Martins[1,2,3], Camilla Simmons[1,4], Antonio Heras-Garvin [5], Elena Klippel [5], Florian Krismer [5], Laura Mantoan Ritter [6]*, Nadia Stefanova [5]*#

1. The Brain Centre, Department of Neuroimaging; Institute of Psychiatry, Psychology, and Neuroscience; King's College London
2. Department of Clinical Neurosciences and Mental Health, Faculty of Medicine, University of Porto, Portugal
3. RISE-Health (Neurosciences), Faculty of Medicine, University of Porto, Portugal
4. Sygnature Discovery, Nottingham, United Kingdom
5. Division of Neurobiology, Department of Neurology, Medical University Innsbruck, Austria
6. Maurice Wohl Clinical Neuroscience Institute, Institute of Psychiatry, Psychology and Neuroscience; King's College London and Clinical Neurosciences Department, King's College Hospital, London

*Contributed equally

#corresponding author: Nadia Stefanova, Division of Neurobiology, Department of Neurology, Medical University of Innsbruck, Innrain 66/G3, 6020 Innsbruck, Austria, E-mail: nadia.stefanova@i-med.ac.at; ORCID: 0000-0001-8188-639X

ABSTRACT

Background: Multiple system atrophy (MSA) is a rapidly progressive α-synucleinopathy characterized by parkinsonism, cerebellar ataxia, and autonomic dysfunction associated with widespread oligodendroglial α-synuclein inclusions, gliosis, and neurodegeneration. Although magnetic resonance imaging (MRI) has revealed characteristic patterns of brain atrophy and microstructural alterations in MSA, the molecular and cellular mechanisms underlying these imaging abnormalities remain poorly understood. The proteolipid protein–human α-synuclein (PLP-αSyn) transgenic mouse model reproduces key pathological and behavioral features of MSA and provides a valuable platform to dissect the biological substrates of MRI-detected changes and their relevance to disease mechanisms.

Methods: We performed the first whole-brain MRI characterization of the PLP-αSyn model using ex vivo structural and diffusion tensor imaging (DTI). To elucidate the molecular mechanisms associated with imaging alterations, we applied an imaging transcriptomics framework integrating MRI-derived phenotypes with more than 4,000 spatial gene expression maps from the Allen Brain Atlas. Gene ontology and cell-type enrichment analyses identified biological processes and cellular contributors linked to MRI changes, and imaging-correlated genes were compared with differentially expressed genes from cerebellar RNA sequencing (RNAseq) to assess molecular concordance.

Results: PLP-αSyn mice exhibited widespread brain atrophy involving the brainstem, cerebellum, thalamus, and white matter tracts, closely mirroring neuroimaging findings in patients with MSA. DTI revealed decreased fractional anisotropy in major white matter tracts and increased mean diffusivity in the brainstem and cerebellum, reflecting distinct microstructural pathologies. Imaging transcriptomics linked these alterations to genes regulating myelination, gliogenesis, and neuroinflammation, strongly enriched for oligodendrocyte and astrocyte markers, while diffusivity changes were associated with neuronal connectivity and energy metabolism. Imaging-correlated gene signatures showed

significant overlap with RNAseq–derived molecular profiles, reinforcing the biological validity of the imaging-derived mechanisms.

Conclusions: MRI sensitively detects MSA-like neurodegeneration in the PLP-αSyn mouse, providing a translationally relevant platform to investigate the biological basis of imaging biomarkers. Integrating MRI with spatial transcriptomics reveals distinct molecular and cellular mechanisms underlying MRI-detected alterations, advancing mechanistic understanding of MRI changes in MSA and establishing imaging transcriptomics as a powerful approach to bridge neuroimaging with molecular pathology in α-synucleinopathies.

Keywords

MRI, DTI, imaging transcriptomics, RNAseq, α-synuclein, multiple system atrophy, disease mechanisms

BACKGROUND

Multiple system atrophy (MSA) is a rapidly progressive neurodegenerative disorder characterized by autonomic failure, parkinsonism, and cerebellar ataxia. Its etiology remains unclear, diagnosis is challenging, and no effective disease-modifying therapy is currently available [1]. MSA is classified as an α-synucleinopathy due to the hallmark accumulation of α-synuclein (α-syn) fibrils within oligodendrocytes, forming glial cytoplasmic inclusions (GCIs) [2].

Animal models have been instrumental in elucidating the molecular and cellular mechanisms of α-syn–mediated oligodendrogliopathy and neurodegeneration [3]. The proteolipid protein (PLP)-αSyn transgenic mouse model of MSA was generated by targeted overexpression of human α-syn under the PLP promoter, driving expression in oligodendrocytes [4]. This model recapitulates key neuropathological and behavioral features of human MSA. α-Syn overexpression induces early oligodendroglial dysfunction, neurotrophic deficits, and progressive α-syn aggregation, leading to GCI-like inclusions, microglial activation, selective neuronal loss, and both motor and non-motor deficits [3, 5].

Neurodegeneration in PLP-αSyn mice begins as early as two months of age, with neuronal loss in brainstem nuclei such as the pedunculopontine and laterodorsal tegmental nuclei [6]. Between 4 and 12 months, pathology progresses to involve the nucleus ambiguus [7], substantia nigra pars compacta, striatum [5], locus coeruleus [8], Barrington nucleus/pontine micturition center [9], and raphe nuclei [10], whereas neurons in the olfactory bulb remain unaffected [11]. Microglial activation evolves in a region- and time-dependent manner, appearing first in the substantia nigra and cerebellar white matter and later in the striatum and lower brainstem [5, 8]. In advanced stages, microglia exhibit disease-associated dysfunction [5, 8]. Cerebellar structures show pronounced vulnerability and stress sensitivity [8, 12-14]. Overall, the regional pattern of neurodegeneration in PLP-αSyn mice closely parallels human MSA pathology [15, 16], making this model a valuable preclinical tool for studying disease mechanisms and evaluating candidate therapies.

Structural neuroimaging plays a critical role in the clinical diagnosis and monitoring of MSA [17]. Automated volumetric, diffusion tensor, and multimodal MRI approaches have been proposed to aid early differential diagnosis [18] and serve as biomarkers of disease progression [19, 20]. Conventional MRI demonstrates region-specific brain atrophy, while diffusion-weighted imaging reveals increased diffusivity in affected regions [20] (**Table 1**). Beyond their diagnostic value, MRI changes may reflect underlying molecular and cellular pathology. A recent study applying imaging transcriptomics — an approach that integrates MRI-derived statistical maps with spatial gene expression atlases — linked brain atrophy in human MSA to overexpression of genes involved in mitochondrial dysfunction, oligodendroglial impairment, and altered neurotransmitter signaling [21]. Imaging transcriptomics investigates spatial patterns of regional vulnerability: it asks why certain brain areas are structurally or functionally more affected by disease, and whether these regional differences can be explained by their normative molecular architecture. By correlating imaging-derived phenotypes with spatial gene-expression gradients, this framework reveals molecular pathways that shape the topography of neurodegeneration. This approach has been increasingly applied in neurodegeneration research to connect macroscopic imaging patterns with molecular processes. For example, imaging–transcriptomic models in Alzheimer's disease have identified gene associations enriched for synaptic, immune, and myelination pathways [22], while in Parkinson's disease and related α-synucleinopathies, they have linked regional MRI changes to genes involved in mitochondrial, inflammatory, and lysosomal pathways [23]. More broadly, imaging transcriptomics provides a powerful tool for bridging neuroimaging biomarkers with the underlying biological mechanisms of neurodegeneration [24].

To date, MRI alterations in the brain of the PLP-αSyn mouse model have not been characterized, limiting our understanding of how the molecular and cellular mechanisms underlying experimental MSA relate to the human disease. In this study, we applied an imaging transcriptomics framework by correlating ex vivo MRI-derived phenotypes of PLP-αSyn mice with over 4,000 spatial gene expression maps from the Allen Brain Atlas. This

integrative analysis enabled the identification of genes whose spatial expression patterns corresponded to MRI-detected alterations, followed by gene enrichment analyses to determine the associated biological processes and cell types [24-26]. To further support these findings, we compared imaging-linked gene expression profiles with differential gene expression data obtained from RNAseq of postmortem brain tissue of the same animal model, thereby bridging macroscopic imaging changes with underlying molecular signatures of neurodegeneration in MSA.

METHODS

Animals

This study included nine female PLP-αSyn mice (four 10-month-old and five 15-month-old) and nine age-matched female wild-type (WT) mice (six 11-month-old and three 15-month-old). The animals were bred and aged in the Animal Facility of the Medical University Innsbruck under temperature-controlled pathogen-free conditions with a light/dark 12-hour cycle and free access to food and water. Mice were anesthetized with an overdose of thiopental and intracardially perfused with phosphate buffered saline (PBS pH□7.4, Sigma-Aldrich, Vienna, Austria) followed by 4% paraformaldehyde (PFA, pH□7.4, Sigma-Aldrich, Vienna, Austria). The heads were removed, postfixed in 4% paraformaldehyde for 24h at 4°C and stored in PBS with 0.05% sodium azide until scanning. All experiments were performed according to the ethical guidelines with the permission of the Austrian Federal Ministry of Science and Research (BMFWF-2022-0.899.398).

The sample size (n = 9 per group) was determined using the resource equation method, which ensures an efficient balance between statistical validity and ethical reduction principles [27]. In this design, the calculated error degrees of freedom (E = total number of animals – total number of groups = 18 − 2 = 16) fall within the acceptable range of 10 ≤ E ≤

20, indicating adequate power for detecting biologically meaningful effects while minimizing unnecessary animal use. The chosen group size is consistent with previous preclinical MRI studies in transgenic models of neurodegeneration. Only female mice were included to reduce variability associated with sex differences in brain structure.

Magnetic resonance imaging

Image acquisition

Skulls were placed four at a time in a 50-ml Falcon tube, separated and secured by a custom 3D-printed holder, and immersed in perfluoropolyether (Galden®, Solvay). These were scanned in a 9.4T Bruker BioSpec 94/20 preclinical MRI scanner with a 39-mm radio-frequency coil to acquire T2-weighted (T2w) structural images and diffusion tensor imaging (DTI) data as previously described [28]. In brief, T2w images with 100-micron isotropic voxel size were acquired with a 3D fast spin echo sequence, and DTI images with 200-micron isotropic voxel size were acquired with a 2D multi-slice pulsed gradient spin echo sequence (4 b0 images, 30 diffusion directions, b=1500 s/mm2).

Image processing and analysis

Diffusion tensor fitting was performed using the dtifit command in FMRIB Software Library (FSL version 5.0.10). Multi-modal study-specific templates were created from the resulting fractional anisotropy (FA) and mean diffusivity (MD) maps and the T2w images using the antsMultivariateTemplateConstruction2.sh script included in Advanced Normalization Tools (ANTs version 2.2.0). Template and individual subject brain masks were created by multiplying the reciprocal of the MD map and the T2w image (fslmaths) and passing this image product to the Rapid Automatic Tissue Segmentation (RATS) tool for skull-stripping of rodent brain MRI [29, 30]. Masked subject images were registered to the masked templates using antsRegistration to perform sequential rigid-body, affine, and diffeomorphic SyN multi-

modal registrations with equal weight given to the FA, MD, and T2w images. To quantify inter-subject voxel-level variations in local brain volume, maps of the Jacobian determinants of the composite transformations were computed using the ANTs CreateJacobianDeterminantImage command. The registered FA and MD maps were smoothed with a full-width half-maximum of 0.2 mm using the 3dBlurInMask command in the Analysis of Functional NeuroImages (AFNI) software suite (version 17.2.17). Univariate, 2×2 ANOVAs were performed on the log-transformed Jacobian determinant maps and the smoothed DTI maps to test for the effects of age (old vs. middle age) and genotype (PLP-αSyn vs. WT) on volume, FA, and MD. This was done using FSL's randomise tool for nonparametric permutation inference to perform 10,000 permutations, threshold-free cluster enhancement, and family-wise error correction.

For region-of-interest (ROI)-based analysis, the masked T2w study template was registered to the Allen Mouse Brain Common Coordinate Framework (CCFv3) using antsRegistration as described above. The CCFv3 atlas labels were merged into 87 ROIs and warped to study template space. ROI volumes were computed by taking the sum of all Jacobian determinant values within each ROI and multiplying by the volume of one voxel. Mann-Whitney U (MWU) tests were performed to compare ROI volumes and mean FA and MD values from the PLP-αSyn and WT groups. The Benjamini-Hochberg procedure was used to correct for multiple comparisons (87 ROIs) for each MRI parameter.

Spatial gene enrichment analysis

Given the limited sample size, all mice (10-15 months of age) were pooled and only the main effects of genotype were considered for spatial gene enrichment analysis. Only the coronal dataset of the Allen *in situ* hybridization data was used because, although it contains far fewer genes than the sagittal dataset, it has superior brain coverage and quality. After excluding gene expression energy maps that had missing data in greater than 20% of voxels

within the brain, the final number of maps included in the analysis was 4071 (some genes have duplicates, which were treated separately and all kept for correlation analysis).

Spatial transcriptomic correlation

The volume, FA, and MD t-statistic maps generated by randomise were warped to CCFv3 space and down-sampled to 200-micron isotropic voxel size to match the gene expression energy maps. The Spearman correlation coefficient (ρ) was calculated between each MRI t-statistic map and each gene expression energy map.

To calculate non-parametric p-values for the ρ values, the BrainSMASH Python package [31] was used to generate 5000 surrogate maps that match the spatial autocorrelation of each of the volume, FA, and MD t-statistic maps. The Spearman correlation coefficient was computed between each surrogate map and each gene expression energy map to build null distributions from which p-values were computed (**Suppl. Fig. S1**).

Gene set enrichment analysis

Two separate gene set enrichment analyses were performed using two categories of gene sets: gene sets associated with the Gene Ontology (GO) biological process terms, and cell-type specific expression (CSE) gene sets curated by Dougherty et al. [32].

For each of 27 different cell types, the authors identified genes that are enriched in that cell population. Further, they truncated these gene lists at four Specificity Index thresholds (pSI) (a smaller pSI corresponds to a more exclusive list of genes that are more specific to a particular cell type) (http://doughertytools.wustl.edu/CSEAtool.html). Two cell types—cone and rod cells—were deemed irrelevant to this study and excluded.

For each type of analysis, only genes found in both the filtered Allen coronal dataset and the GO or CSE gene sets were included, resulting in 3606 and 3646 expression maps of 3385 and 3422 unique genes, respectively. The GO biological process terms were filtered by removing those with fewer than 10 or more than 200 remaining genes, à la Ritchie [33].

Furthermore, terms with identical gene sets (exactly equal) to another term were discarded, leaving a final count of 2393 GO biological process terms. The curation of the GO and CSE gene sets were performed with custom Python scripts.

For each MRI parameter, genes were ranked by FDR-corrected p-value and then by the absolute value of ρ. For genes with duplicates, only the highest ranked duplicate was kept for gene set enrichment analysis. The minimum hypergeometric (mHG) score [34] was used to quantify the enrichment of GO and CSE gene sets at the top of these ranked lists. To account for propagating effects of spatial autocorrelation into the enrichment analysis, a null distribution of mHG scores for each MRI parameter and gene set pair was calculated from the BrainSMASH-derived surrogate maps. For each observed mHG score s, a p-value was calculated as the fraction of mHG scores in the corresponding null distribution $s' < s$. To control the false discovery rate in each MRI parameter, the Benjamini-Hochberg procedure was performed across: 1) all 2393 GO gene sets, 2) the 42 GO gene sets that contain Plp1, and 3) the 25 CSE gene sets for each pSI level.

Imaging transcriptomics and RNAseq correlation

To consolidate the relevance of the disease-associated gene maps defined by imaging transcriptomics, we identified the significantly correlated genes to volume, FA and MD ($p<0.05$), which are found significantly dysregulated in the PLP-αSyn cerebellum by RNAseq and DESeq2 analysis ($p_{adj}>0.05$,[13]). We calculated the Spearman correlation of the Spearman ρ values from the imaging transcriptomics and the Log2(FC) values from the DESeq2 analysis applying GraphPad Prism 10.5.0 software. In addition, we performed the enrichment analysis described above using the significantly dysregulated genes as a gene set. Of the 3494 genes found in both the Allen Atlas and RNAseq datasets, 758 genes were differentially expressed and considered in this enrichment analysis.

RESULTS

Multiparametric MRI identifies atrophy and microstructural alterations in the MSA mouse brains

Ex vivo deformation-based morphometry revealed widespread brain atrophy in PLP-αSyn mice compared with age-matched WT controls (**Figure 1a; Suppl. Fig. S2a**). Significant age × genotype interactions were detected in some regions; therefore, post hoc comparisons were performed. At 10 months, PLP-αSyn mice exhibited pronounced volume loss in the midbrain, hindbrain, and cerebellum, accompanied by ventricular enlargement, consistent with neurodegeneration. Conversely, localized volume increases were observed in regions of the cortex, amygdala, and striatum (**Suppl. Fig. S2a**). By 15 months, atrophy extended to additional brain areas, and no regions displayed volume gain (**Suppl. Fig. S2b**). This pattern was at least partly associated with an age-related volume increase in WT mice (**Suppl. Fig. S2c**).

Given the limited group sizes and the absence of age or age × genotype effects in the diffusion metrics (FA and MD), subsequent analyses focused on the main genotype effect. Significant atrophy was identified in multiple motor-related structures, including the pons, extrapyramidal fiber tracts, medulla, pedunculopontine tegmental nucleus, and cerebellum (**Table 2; Figure 2a**). Non-motor regions implicated in sleep regulation, autonomic control, anxiety, and pain processing—such as the epithalamus, ventral tegmental area, raphe nuclei, insular cortex, reticular nucleus, and intralaminar thalamic nuclei—also showed reduced volume (**Suppl. Fig. S3a**).

FA was reduced across widespread white-matter tracts (**Table 2; Suppl. Fig. S3b**), including interhemispheric pathways (anterior commissure, corpus callosum), descending motor tracts (internal capsule, cerebellar peduncles), and fibers associated with non-motor systems (optic nerve, olfactory bulb, epithalamus, stria terminalis) (**Table 2; Figure 2b**). In contrast, MD was globally increased, with the most significant elevations in the brainstem and cerebellum (**Table 2; Figure 2c; Suppl. Fig. S3c**).

Imaging transcriptomics links MRI phenotypes to gene expression signatures of myelination, gliogenesis, neuroinflammation, and neural network regulation

To relate MRI changes to underlying molecular mechanisms, we performed imaging transcriptomic analyses, examining spatial correlations between MRI-derived t-statistic maps (volume, FA, MD) and normative gene expression patterns from the Allen Brain Atlas. We identified 3,214 genes significantly correlated with regional volume changes ($p_{adj} < 0.05$), 1,850 with FA, and 2,334 with MD (**Suppl. Tables S1–S3**). All correlations exceeded those expected by chance ($p = 0$ vs. 5,000 BrainSMASH surrogates). The top 30 volume- and top 55 FA-correlated genes were predominantly negatively associated with the corresponding MRI features, while among the top 60 MD-correlated genes, 20 showed positive associations (**Suppl. Tables S1–S3**).

Genes most strongly correlated with atrophy included *Arhgef10* (axon guidance, nerve conduction), *Cldn11* (axon ensheathment), *Tspan2* (oligodendrocyte differentiation), *Aspa* (N-acetylaspartate metabolism relevant to myelin synthesis), *Cnp* (myelinating cell RNA regulation), *Ugt8a* (galactocerebroside synthesis), and *Fa2h* (myelin sphingolipid biosynthesis). Top FA-correlated genes overlapped substantially, featuring *Cldn11*, *Tspan2*, *Cnp*, and *Fa2h*, alongside immune and proteostasis regulators (*Lpar1*, *CD9*, *App*, *Adamts4*, *Cryab*). MD-correlated genes included neuronal and metabolic markers such as *Pvalb* (inhibitory interneurons), *Scn1a* (neuronal excitability), *Uqcrh* (mitochondrial respiration), and *Abcd2* (energy metabolism).

To assess the direct contribution of the PLP-driven human α-synuclein overexpression, we correlated MRI t-statistic maps with *Plp1* expression (**Figure 3**). Volume and FA maps exhibited negative correlations with *Plp1*, indicating that MRI-detected reductions in these metrics likely reflect oligodendroglial dysfunction and myelination deficits directly linked to α-synuclein overexpression. In contrast, MD showed no association with *Plp1*, suggesting that

diffusivity changes may represent downstream or compensatory mechanisms involving non-oligodendroglial pathways, consistent with enrichment for neuronal and mitochondrial genes. Gene Ontology (GO) enrichment analysis of FA-correlated genes revealed significant (FDR < 0.05) overrepresentation of processes related to myelination, gliogenesis, and astrocyte and oligodendrocyte differentiation, all prominently featuring *Plp1* (**Figure 4; Suppl. Tables S4–S5**). By contrast, genes associated with MD changes were enriched only for dendritic spine development, a process not containing *Plp1*, consistent with secondary, neuronally driven responses (**Suppl. Table S6**).

Cell-type enrichment implicates oligodendrocytes, astrocytes, and specific neuronal subpopulations

Cell-type–specific enrichment analysis demonstrated that genes spatially correlated with regional volume loss were significantly enriched (FDR < 0.05) for oligodendrocyte markers in the cortex and cerebellum, and for cholinergic neurons of the spinal cord and brainstem (**Figure 5a; Suppl. Table S10**). Subthreshold enrichment ($0.05 < p < 0.1$) was observed for brainstem serotonergic neurons.

Similarly, genes correlated with FA reduction were enriched for cortical and cerebellar oligodendrocytes, cerebellar stellate and basket cells, and Purkinje cells (pSI < 0.001), as well as cortical and cerebellar astrocytes and oligodendrocyte progenitors (pSI < 0.05) (**Figure 5b; Suppl. Table S11**). Subthreshold enrichment was observed for Bergmann glia and cerebellar granule cells. No cell type reached significance for genes associated with increased MD (**Figure 5c; Suppl. Table S12**), although mild enrichment was noted for cortical layer 6 pyramidal cells and prepronociceptin (PNOC)-expressing neurons.

RNAseq supports the biological relevance of molecular signatures of neurodegeneration identified by imaging transcriptomics

To test if the genes we have identified indirectly to be associated with disorder-related imaging phenotypes are indeed dysregulated in the post-mortem brain tissue of the same model, we performed RNAseq and DESeq2 analysis on cerebellar tissue from PLP-αSyn mice [13] and cross-referenced the 2613 differentially expressed genes (DEGs, FDR<0.05) with those correlated to MRI-derived maps. We identified 664 DEGs overlapping with volume-correlated genes, 441 with FA-correlated genes, and 510 with MD-correlated genes (**Suppl. Tables S7-S9**). The log2(FC) values of cerebellar DEGs were weakly but significantly correlated with FA-correlated genes (ρ =-0.106, p=0.026) and MD-correlated genes (ρ=-0.1895, p<0.0001) (**Figure 6**). Further enrichment analysis showed that the DEGs were significantly overrepresented (p=0.0376) among the genes whose normative spatial expression patterns correlated most strongly with volume changes in the PLP-αSyn mice (**Table 3**). The overlap between DEGs and MRI-correlated genes supports the biological relevance of the imaging transcriptomics findings and links MRI-detected alterations to molecular signatures of neurodegeneration in MSA.

DISCUSSION

The PLP-αSyn mouse model of MSA recapitulates key pathological and clinical hallmarks of the human disease, including progressive motor and non-motor deficits, oligodendroglial α-synuclein inclusions, widespread gliosis, and neuronal loss. Previous work has established its utility for elucidating α-synuclein–driven mechanisms and testing disease-modifying therapies, which mitigate α-synuclein aggregation, neuroinflammation and preserve neuronal populations [12, 35-40].

In the present study, we provide the first comprehensive, whole-brain MRI characterization of the PLP-αSyn mouse compared with wild-type controls. Using ex vivo structural MRI, we

identified a reproducible pattern of regional atrophy encompassing white matter tracts, the brainstem (medulla, pons, midbrain), cerebellum, thalamus, hypothalamus, and subiculum (**Fig. 1a, Suppl. Fig. S3a**). The distribution of volume loss mirrored the neuroimaging phenotype reported in patients with MSA [20, 41, 42], including involvement of the hippocampus, pons, medulla, cerebellum, and pyramidal tracts (**Table 1**). This close correspondence reinforces the translational relevance of MRI-detected neurodegeneration in the PLP-αSyn model.

DTI further revealed widespread microstructural alterations. FA was decreased in major white-matter tracts, including the corpus callosum, fornix, anterior commissure, striatothalamic fibers, and cerebellar peduncles—changes that parallel those observed in clinical MSA (**Table 1**). These FA reductions likely reflect subtle alterations in myelination and axon–glia interactions rather than overt demyelination, consistent with previous ultrastructural studies in this model. Localized FA increases detected in the hippocampus likely represent maladaptive tissue reorganization associated with gliosis or selective loss of crossing fibers. MD, by contrast, was predominantly elevated in the brainstem and cerebellum, reflecting tissue rarefaction, increased extracellular water, and axonal pathology. The limited spatial overlap between FA and MD alterations suggests that these metrics capture distinct aspects of the underlying pathology—microstructural disorganization versus extracellular matrix and cellular composition changes. Our observations further support the role of neuroimaging in addressing the biological substrate of neurodegenerative disorders [43, 44].

To probe the molecular mechanisms underlying these MRI phenotypes, we applied an imaging transcriptomics framework integrating spatial MRI maps with brain-wide gene expression data from the Allen Brain Atlas. This approach revealed robust associations between imaging alterations and genes involved in myelination, gliogenesis, and neuroinflammation—biological processes central to oligodendroglial dysfunction in MSA. Notably, FA and volume changes, but not MD, were significantly correlated with *Plp1* expression, indicating that these MRI signatures are tightly linked to the oligodendrocyte-

specific overexpression of human α-synuclein and the resulting GCI pathology [5]. In contrast, the absence of correlation between MD and *Plp1* suggests that MD increases may reflect downstream, neuronally mediated processes involving energy metabolism and mitochondrial function.

Gene Ontology analyses reinforced these findings: FA- and volume-related gene sets were enriched for myelination, gliogenesis, and astrocyte differentiation, whereas MD-correlated genes were enriched only for dendritic spine development, further underscoring their distinct mechanistic underpinnings. Cell-type–specific enrichment supported this interpretation, highlighting significant contributions of cortical and cerebellar oligodendrocytes and astrocytes to the FA and volume changes, with additional involvement of cholinergic and serotonergic neurons.

We further supported the biological relevance of the imaging transcriptomics findings by comparing them with DEG profiles derived from RNAseq of cerebellar tissue from PLP-αSyn mice [13]. The overlapping enrichment for genes regulating axon guidance, synaptic transmission, calcium signaling, oxidative stress, immune activation, and lipid metabolism provides strong molecular corroboration for the imaging-derived associations. Together, these results suggest that MRI-based phenotypes in the PLP-αSyn mouse capture a spectrum of processes encompassing oligodendroglial dysfunction, neuroinflammation, and metabolic stress—core features of MSA pathology [2].

Although histological confirmation was beyond the scope of this work, the spatial alignment of MRI-detected alterations with known sites of neurodegeneration in the PLP-αSyn mouse supports the biological validity of these imaging markers [5-9]. Importantly, our findings parallel a recent imaging transcriptomics study in human MSA brains [21], which identified overlapping atrophy patterns in the cerebellum, pons, and midbrain and revealed enrichment for genes related to mitochondrial function, energy metabolism, and myelin integrity. The convergence of molecular and anatomical signatures across species underscores the translational robustness of the PLP-αSyn model and validates the use of multiparametric MRI and imaging transcriptomics for dissecting mechanisms of neurodegeneration.

Some limitations should be acknowledged. First, imaging was performed ex vivo on a modest sample size and limited to female mice; while this approach provides high spatial resolution, it precludes longitudinal assessment of disease progression and may introduce fixation-related bias. Future studies should incorporate longitudinal in vivo MRI to monitor dynamic changes across disease stages and assess treatment effects. Second, the imaging-transcriptomic correlations rely on the Allen Brain Atlas, which represents gene expression in healthy brains. Thus, inferred molecular associations may underestimate disease-specific transcriptional alterations. Integration with single-cell and spatial transcriptomics datasets from MSA models or human post-mortem tissue will improve biological specificity [45]. While the histopathological validation and attribution of MRI changes is partly based on earlier observations [5-7, 9, 13], combining MRI with quantitative spatial proteomics will help delineate the cellular substrates of each imaging marker in future studies. Finally, the cross-sectional design limits causal inference about the temporal hierarchy of oligodendroglial and neuronal changes. Future studies should employ time-resolved imaging and transcriptomic profiling alongside experimental manipulations - such as conditional gene targeting or pharmacological interventions - to establish causal links between cellular dysfunction and MRI-derived phenotypes.

CONCLUSIONS

This study demonstrates that structural and diffusion MRI sensitively detect widespread neurodegenerative changes in the PLP-αSyn mouse model of MSA that closely mirror human disease patterns. Through imaging transcriptomics, we linked these MRI phenotypes to gene expression signatures related to myelination, gliogenesis, neuroinflammation, and neuronal network regulation, which were further supported by RNAseq analysis. The strong correspondence between imaging–molecular associations in experimental and clinical MSA highlights the translational relevance of the PLP-αSyn model. Our findings establish MRI combined with spatial transcriptomic integration as a powerful framework for uncovering

molecular drivers of imaging phenotypes in neurodegenerative disease models. Future longitudinal in vivo studies should assess the capacity of MRI to track disease progression and therapeutic responses, enabling more predictive preclinical evaluation of candidate interventions for MSA and related α-synucleinopathies.

List of abbreviations

DEGs, differentially expressed genes

DTI, diffusion tensor imaging

FA, fractional anisotropy

FWER, family-wise error rate

GCIs, glial cytoplasmic inclusions

MD, mean diffusivity

MRI, magnetic resonance imaging

MSA, Multiple system atrophy

PFA, paraformaldehyde

PLP-αSyn, proteolipid protein–human α-synuclein

RNAseq, RNA sequencing

WT, wild-type

α-syn, α-synuclein

Tables

Table 1: Regions of interest with significantly altered MRI volumes and diffusivity in human MSA compared to healthy controls.

Brain region	**MRI**			
	volume	**FA**	**MD**	*Ref.*
Cerebral white matter	↑	↓	↑	*[46-51]*
Amygdala	-	↓	-	*[52]*
Pyramidal tract	↓	↓	↑	*[47, 53-59]*
Capsula interna	-	↓	↑	*[46-48, 53, 55, 60, 61]*
Putamen/Striatum	↓	↓	↑	*[17, 46, 52, 54, 62-71]*
Globus pallidus	-	↑	-	*[52, 70]*
Midbrain	↓	↓	↑	*[48, 68, 70, 72, 73]*
Cerebral peduncle		↓	↑	*[48, 61]*
Substantia nigra	↓	↓	-	*[52, 66, 68, 74, 75]*
Red nucleus	-	-	↑	*[52]*
Subthalamic nucleus	-	-	↑	*[52]*
Brainstem	-	-	↑	*[76]*
Medulla	↓	-	-	*[66]*
Pons	↓	↓	↑	*[17, 47, 48, 54, 55, 58, 60, 61, 66, 68-70, 72, 74, 77-81]*
Cerebellum	gray matter: ↓ white matter: ↑/↓ total: ↓	↓	↑	*[17, 48-52, 54-56, 58, 62, 63, 66, 68-70, 76, 79, 80, 82, 83]*
Middle cerebellar peduncle (MCP)	↓	↓	↑	*[17, 46-48, 52, 54-56, 58-60, 66, 68-70, 77, 79, 84-88]*
Superior cerebellar peduncle (SCP)	-	↓	↑	*[46-48, 70, 87]*

↑ = significantly increased
↓ = significantly decreased
- = no data available
FA = fractional anisotropy
MD = mean diffusivity

Table 2. Most affected brain regions according to atlas-based statistics comparing PLP-αSyn and wild-type mice.

volume			FA			MD		
ROI	**% difference in group medians**	**FDR-corrected p-value**	**ROI**	**% difference in group medians**	**FDR-corrected p-value**	**ROI**	**% difference in group medians**	**FDR-corrected p-value**
epithalamus related	-8.89	0.004	anterior commissure, olfactory limb	-12.32	5.10E-04	Pons, behavioral state related	4.86	0.05
Perithalamus	-14.15	0.004	optic nerve	-12.59	5.10E-04	Cerebellar nuclei	4.16	0.054
Ventral tegmental area	-19.98	0.004	thalamus related	-13.64	5.10E-04	Red nucleus	7.08	0.054
Raphe nuclei	-14.7	0.004	fornix system	-13.59	5.10E-04	(Para)flocculus	7.96	0.054
Pons, sensory related	-11.73	0.004	epithalamus related	-13.33	5.10E-04	Cerebellar vermis	8.84	0.064
Pons, motor related	-10.33	0.004	lateral ventricle	-19.32	5.10E-04	Cerebellar hemispheres	15.12	0.115
medial lemniscus	-12.7	0.004	third ventricle	-14.36	5.10E-04	Inferior colliculus	9.6	0.18
extrapyramidal fiber systems	-11.97	0.004	corpus callosum	-13.08	7.20E-04	third ventricle	19.3	0.18
Insular cortex	7.82	0.005	fourth ventricle	-9.03	7.20E-04	Pedunculotegmental nucleus	5.36	0.18
Reticular nucleus	-11.5	0.005	choroid plexus	-18.24	7.20E-04	arbor vitae	3.87	0.18
Medulla, motor related	-10.04	0.005	stria terminalis	-13.1	0.001	Pons, motor related	4.07	0.217
Intralaminar thalamic nuclei	-10.82	0.006	Olfactory bulb	-6.93	0.003	Ventral thalamus	5.39	0.228
Pedunculotegmental nucleus	-9.34	0.006	Geniculate nucleus	-9.51	0.003	facial nerve	4.08	0.241
cerebellar peduncles	-14.15	0.006	Perithalamus	-9.83	0.003	Raphe nuclei	5.49	0.288
internal capsule	-17.15	0.007	Pretectal region	-13.58	0.003	lateral ventricle	36.01	0.292
Pons, behavioral state related	-9.64	0.008	Superior colliculus	-9.94	0.003	oculomotor nerve	5.18	0.319
Cerebellar nuclei	-15.68	0.008	arbor vitae	-9.3	0.003	Medulla, sensory related	2.72	0.319
vestibulocochlear nerve	-13.28	0.008	internal capsule	-9.75	0.004	corticospinal tract	-2.03	0.319
stria terminalis	-9.81	0.013	Cerebellar hemispheres	-10.74	0.005	Primary somatosensory cortex	6.51	0.319
Cuneiform nucleus	-6.82	0.016	Cerebellar nuclei	-4.42	0.007	Habenula	8.99	0.319

Table 3. Cerebellar DEG enrichment analysis.

MRI parameter	N	B	b	n	enrichment	smHG	p-value
volume	3494	758	146	504	1.33529128	1.96E-05	0.0376
FA	3494	758	9	18	2.30474934	0.00735212	0.3692
MD	3494	758	5	6	3.8412489	0.00234034	0.2398

DEG: differentially expressed gene, N: total number of genes found in both the Allen Atlas and RNAseq datasets, B: number of DEGs in the N total genes, b: number of DEGs in the top n ranked genes, enrichment = (b/n)/(B/N), smHG: minimum hypergeometric test statistic, FA: fractional anisotropy, MD: mean diffusivity

SUPPLEMENTARY MATERIAL

Additional file 1

Title: Supplementary Figures: Fig S1 to S3.

Format: .pdf

Additional file 2

Title: Supplementary Tables: Tables S1 to S12.

Format: .xls

Declarations

Ethics approval and consent to participate

All in vivo experiments were performed according to the ARRIVE guidelines with the permission of the Austrian Federal Ministry of Science and Research (BMFWF-2022-0.899.398).

Consent for publication

Not applicable

Availability of data and materials

All data generated or analysed during this study are included in this published article and its supplementary information files.

Competing interests

EK, declares no competing interests

DC, declares no competing interests

DM, declares no competing interests

CS, declares no competing interests

EK, declares no competing interests

AHG, received grant support from the Austrian Science Fund (FWF) and the Tyrolian Science Fund (TWF) outside of the submitted work.

FK, received personal fees from AbbVie, Bial, Ionis Pharmaceuticals, Koneksa, Merz, Österreichische Apotheker-Verlagsgesellschaft, Sanofi, Takeda Pharmaceuticals, and Teva and his institution has ongoing grant support from the Austrian Science Fund (FWF), the National Institutes of Health and the Michael J. Fox Foundation, outside of the submitted work.

LM, declares no competing interests

NS, received grant support from the Medical University of Innsbruck and The Michael J. Fox Foundation, outside of the submitted work; Director-at-large, Board of Directors and Chair of the Research Steering Council of Mission MSA, USA; Advisory board, Karl Golser Foundation, Italy; Advisory services for IONIS, Mitsubishi Pharma

Authors' contributions

EK has contributed to the methodology, data analysis of the study and drafting parts of the manuscript

DC has contributed to the conceptualization of the study, data interpretation, and drafting parts of the manuscript

DM has contributed to the methodology of the study

CS has contributed to the methodology of the study

EK has contributed by summarizing clinical MRI/DTI studies in MSA

AHG has contributed to data analysis and tissue preparation

FK has contributed to the interpretation of the clinical relevance of the data

LM has contributed to the conceptualization of the study

NS has contributed to the conceptualization of the study, analysis of the data, data interpretation, and drafting parts of the manuscript

All authors have reviewed and approved the final version of the manuscript.

References

1. Poewe W, Stankovic I, Halliday G, Meissner WG, Wenning GK, Pellecchia MT, et al. Multiple system atrophy. Nat Rev Dis Primers. 2022;8:56.

2. Stefanova N, Wenning GK. Multiple system atrophy: at the crossroads of cellular, molecular and genetic mechanisms. Nat Rev Neurosci. 2023;24:334-346.

3. Stefanova N. A Mouse Model of Multiple System Atrophy: Bench to Bedside. Neurotherapeutics. 2023;20:117-126.

4. Kahle PJ, Neumann M, Ozmen L, Muller V, Jacobsen H, Spooren W, et al. Hyperphosphorylation and insolubility of alpha-synuclein in transgenic mouse oligodendrocytes. EMBO Rep. 2002;3:583-588.

5. Refolo V, Bez F, Polissidis A, Kuzdas-Wood D, Sturm E, Kamaratou M, et al. Progressive striatonigral degeneration in a transgenic mouse model of multiple system atrophy: translational implications for interventional therapies. Acta Neuropathol Commun. 2018;6:2.

6. Stemberger S, Poewe W, Wenning GK, Stefanova N. Targeted overexpression of human alpha-synuclein in oligodendroglia induces lesions linked to MSA-like progressive autonomic failure. Exp Neurol. 2010;224:459-464.

7. Kuzdas D, Stemberger S, Gaburro S, Stefanova N, Singewald N, Wenning GK. Oligodendroglial alpha-synucleinopathy and MSA-like cardiovascular autonomic failure: experimental evidence. Exp Neurol. 2013;247:531-536.

8. Stefanova N, Reindl M, Neumann M, Haass C, Poewe W, Kahle PJ, et al. Oxidative stress in transgenic mice with oligodendroglial alpha-synuclein overexpression replicates the characteristic neuropathology of multiple system atrophy. Am J Pathol. 2005;166:869-876.

9. Boudes M, Uvin P, Pinto S, Voets T, Fowler CJ, Wenning GK, et al. Bladder dysfunction in a transgenic mouse model of multiple system atrophy. Mov Disord. 2013;28:347-355.

10. Flabeau O, Meissner WG, Ozier A, Berger P, Tison F, Fernagut PO. Breathing variability and brainstem serotonergic loss in a genetic model of multiple system atrophy. Mov Disord. 2014;29:388-395.

11. Krismer F, Wenning GK, Li Y, Poewe W, Stefanova N. Intact olfaction in a mouse model of multiple system atrophy. PLoS One. 2013;8:e64625.

12. Cheng A, Kawahata I, Wang Y, Jia W, Wang H, Sekimori T, et al. Epsin2, a novel target for multiple system atrophy therapy via alpha-synuclein/FABP7 propagation. Brain. 2023;146:3172-3180.

13. Heras-Garvin A, Fellner L, Granata R, Wenning GK, Stefanova N. Transcriptional dysregulation in the cerebellum triggered by oligodendroglial alpha-synucleinopathy: insights from a transgenic mouse into the early disease mechanisms of MSA. J Neural Transm (Vienna). 2025;10.1007/s00702-025-02892-5.

14. Stefanova N, Kaufmann WA, Humpel C, Poewe W, Wenning GK. Systemic proteasome inhibition triggers neurodegeneration in a transgenic mouse model expressing human alpha-synuclein under oligodendrocyte promoter: implications for multiple system atrophy. Acta Neuropathol. 2012;124:51-65.

15. Wenning GK, Ben Shlomo Y, Magalhaes M, Daniel SE, Quinn NP. Clinical features and natural history of multiple system atrophy. An analysis of 100 cases. Brain. 1994;117 (Pt 4):835-845.

16. Wenning GK, Tison F, Ben Shlomo Y, Daniel SE, Quinn NP. Multiple system atrophy: a review of 203 pathologically proven cases. Mov Disord. 1997;12:133-147.

17. Wenning GK, Stankovic I, Vignatelli L, Fanciulli A, Calandra-Buonaura G, Seppi K, et al. The Movement Disorder Society Criteria for the Diagnosis of Multiple System Atrophy. Mov Disord. 2022;37:1131-1148.

18. Chougar L, Faucher A, Faouzi J, Lejeune FX, Gama Lobo G, Jovanovic C, et al. Contribution of MRI for the Early Diagnosis of Parkinsonism in Patients with Diagnostic Uncertainty. Mov Disord. 2024;39:825-835.

19. Fabbri M, Del Campo N, Meissner WG, Rousseau V, Sommet A, Payoux P, et al. Disease Progression in Multiple System Atrophy: The ASPIRE Multi-Modal Biomarker Study. Annals of neurology. 2025;10.1002/ana.70028.

20. Krismer F, Seppi K, Poewe W. The role of neuro-imaging in multiple system atrophy. J Neural Transm (Vienna). 2025;10.1007/s00702-025-02964-6.

21. Chougar L, Tremblay C, Delva A, Filiatrault M, Vo A, Hansen JY, et al. Atrophy in multiple system atrophy relates to mitochondrial and oligodendrocytic processes. medRxiv. 2025;10.1101/2025.01.22.25320961:2025.2001.2022.25320961.

22. Adewale Q, Khan AF, Carbonell F, Iturria-Medina Y, Alzheimer's Disease Neuroimaging I. Integrated transcriptomic and neuroimaging brain model decodes biological mechanisms in aging and Alzheimer's disease. Elife. 2021;10.

23. Mroczek M, Desouky A, Sirry W. Imaging Transcriptomics in Neurodegenerative Diseases. J Neuroimaging. 2021;31:244-250.

24. Arnatkeviciute A, Fulcher BD, Bellgrove MA, Fornito A. Imaging Transcriptomics of Brain Disorders. Biol Psychiatry Glob Open Sci. 2022;2:319-331.

25. Martins D, Giacomel A, Williams SCR, Turkheimer F, Dipasquale O, Veronese M, et al. Imaging transcriptomics: Convergent cellular, transcriptomic, and molecular neuroimaging signatures in the healthy adult human brain. Cell Rep. 2021;37:110173.

26. Edwards LJ, McColgan P, Helbling S, Zarkali A, Vaculciakova L, Pine KJ, et al. Quantitative MRI maps of human neocortex explored using cell type-specific gene expression analysis. Cereb Cortex. 2023;33:5704-5716.

27. Charan J, Kantharia ND. How to calculate sample size in animal studies? Journal of pharmacology & pharmacotherapeutics. 2013;4:303-306.

28. White MA, Lin Z, Kim E, Henstridge CM, Pena Altamira E, Hunt CK, et al. Sarm1 deletion suppresses TDP-43-linked motor neuron degeneration and cortical spine loss. Acta Neuropathol Commun. 2019;7:166.

29. Oguz I, Zhang H, Rumple A, Sonka M. RATS: Rapid Automatic Tissue Segmentation in rodent brain MRI. J Neurosci Methods. 2014;221:175-182.

30. Yin Y, Zhang X, Williams R, Wu X, Anderson DD, Sonka M. LOGISMOS--layered optimal graph image segmentation of multiple objects and surfaces: cartilage segmentation in the knee joint. IEEE Trans Med Imaging. 2010;29:2023-2037.

31. Burt JB, Helmer M, Shinn M, Anticevic A, Murray JD. Generative modeling of brain maps with spatial autocorrelation. Neuroimage. 2020;220:117038.

32. Dougherty JD, Schmidt EF, Nakajima M, Heintz N. Analytical approaches to RNA profiling data for the identification of genes enriched in specific cells. Nucleic Acids Res. 2010;38:4218-4230.

33. Ritchie J, Pantazatos SP, French L. Transcriptomic characterization of MRI contrast with focus on the T1-w/T2-w ratio in the cerebral cortex. Neuroimage. 2018;174:504-517.

34. Eden E, Lipson D, Yogev S, Yakhini Z. Discovering motifs in ranked lists of DNA sequences. PLoS Comput Biol. 2007;3:e39.

35. Heras-Garvin A, Refolo V, Schmidt C, Malfertheiner K, Wenning GK, Bradbury M, et al. ATH434 Reduces alpha-Synuclein-Related Neurodegeneration in a Murine Model of Multiple System Atrophy. Mov Disord. 2021;36:2605-2614.

36. Luque M, Matic M, Heras-Garvin A, Amo-Aparicio J, Luk KC, Haindl MT, et al. Pharmacologic NLRP3 Inhibition Modulates Parkinson's Disease-Associated Microglial Transcriptomic Signatures and Mitigates α-Synuclein–Triggered Neurodegeneration. bioRxiv. 2025;10.1101/2025.10.22.683837:2025.2010.2022.683837.

37. Heras-Garvin A, Weckbecker D, Ryazanov S, Leonov A, Griesinger C, Giese A, et al. Anle138b modulates α-synuclein oligomerization and prevents motor decline and neurodegeneration in a mouse model of multiple system atrophy. Mov Disord. 2019;34:255-263.

38. Lemos M, Venezia S, Refolo V, Heras-Garvin A, Schmidhuber S, Giese A, et al. Targeting α-synuclein by PD03 AFFITOPE® and Anle138b rescues neurodegenerative pathology in a model of multiple system atrophy: clinical relevance. Translational neurodegeneration. 2020;9:38.

39. Venezia S, Kaufmann WA, Wenning GK, Stefanova N. Toll-like receptor 4 deficiency facilitates α-synuclein propagation and neurodegeneration in a mouse model of prodromal Parkinson's disease. Parkinsonism Relat Disord. 2021;91:59-65.

40. Venezia S, Refolo V, Polissidis A, Stefanis L, Wenning GK, Stefanova N. Toll-like receptor 4 stimulation with monophosphoryl lipid A ameliorates motor deficits and nigral neurodegeneration triggered by extraneuronal α-synucleinopathy. Molecular neurodegeneration. 2017;12:52.

41. Jost WH, Rau A, Brumberg J, Urbach H, Meyer PT, Schröter N. Neuroimaging in multiple system atrophy: clinical implications and novel developments. J Neural Transm (Vienna). 2025;10.1007/s00702-025-02921-3.

42. Chelban V, Bocchetta M, Hassanein S, Haridy NA, Houlden H, Rohrer JD. An update on advances in magnetic resonance imaging of multiple system atrophy. J Neurol. 2019;266:1036-1045.

43. Mastenbroek SE, Collij LE, Anijärv TE, Rittmo J, Young AL, Strandberg O, et al. Biological classification of memory clinic patients. Brain. 2025;10.1093/brain/awaf411.

44. Haghshomar M, Dolatshahi M, Ghazi Sherbaf F, Sanjari Moghaddam H, Shirin Shandiz M, Aarabi MH. Disruption of Inferior Longitudinal Fasciculus Microstructure in Parkinson's Disease: A Systematic Review of Diffusion Tensor Imaging Studies. Frontiers in neurology. 2018;9:598.

45. Shen J, Liang W, Zhao R, Chen Y, Liu Y, Cheng W, et al. Cross-tissue multi-omics analyses reveal the gut microbiota's absence impacts organ morphology, immune homeostasis, bile acid and lipid metabolism. iMeta. 2025;4:e272.

46. Rulseh AM, Keller J, Rusz J, Syka M, Brozova H, Rusina R, et al. Diffusion tensor imaging in the characterization of multiple system atrophy. Neuropsychiatr Dis Treat. 2016;12:2181-2187.

47. Gorges M, Maier MN, Rosskopf J, Vintonyak O, Pinkhardt EH, Ludolph AC, et al. Regional microstructural damage and patterns of eye movement impairment: a DTI and video-oculography study in neurodegenerative parkinsonian syndromes. J Neurol. 2017;264:1919-1928.

48. Dash SK, Stezin A, Takalkar T, George L, Kamble NL, Netravathi M, et al. Abnormalities of white and grey matter in early multiple system atrophy: comparison of parkinsonian and cerebellar variants. Eur Radiol. 2019;29:716-724.

49. Jao CW, Soong BW, Huang CW, Duan CA, Wu CC, Wu YT, et al. Diffusion Tensor Magnetic Resonance Imaging for Differentiating Multiple System Atrophy Cerebellar Type and Spinocerebellar Ataxia Type 3. Brain Sci. 2019;9.

50. Ge Y, Zheng W, Li Y, Dou W, Ren S, Chen Z, et al. Altered Brain Volume, Microstructure Metrics and Functional Connectivity Features in Multiple System Atrophy. Front Aging Neurosci. 2022;14:799251.

51. Raghavan S, Lesnick TG, Castillo AM, Reid RI, Fought AJ, Thostenson KB, et al. White Matter Abnormalities Track Disease Progression in Multiple System Atrophy. Movement disorders clinical practice. 2024;11:1085-1094.

52. Du G, Lewis MM, Kanekar S, Sterling NW, He L, Kong L, et al. Combined Diffusion Tensor Imaging and Apparent Transverse Relaxation Rate Differentiate Parkinson Disease and Atypical Parkinsonism. AJNR Am J Neuroradiol. 2017;38:966-972.

53. Ito M, Watanabe H, Atsuta N, Senda J, Kawai Y, Tanaka F, et al. Fractional anisotropy values detect pyramidal tract involvement in multiple system atrophy. J Neurol Sci. 2008;271:40-46.

54. Ito M, Watanabe H, Kawai Y, Atsuta N, Tanaka F, Naganawa S, et al. Usefulness of combined fractional anisotropy and apparent diffusion coefficient values for detection of involvement in multiple system atrophy. J Neurol Neurosurg Psychiatry. 2007;78:722-728.

55. Prakash N, Hageman N, Hua X, Toga AW, Perlman SL, Salamon N. Patterns of fractional anisotropy changes in white matter of cerebellar peduncles distinguish spinocerebellar ataxia-1 from multiple system atrophy and other ataxia syndromes. Neuroimage. 2009;47 Suppl 2:T72-81.

56. Wang PS, Wu HM, Lin CP, Soong BW. Use of diffusion tensor imaging to identify similarities and differences between cerebellar and Parkinsonism forms of multiple system atrophy. Neuroradiology. 2011;53:471-481.

57. Ji L, Zhu D, Xiao C, Shi J. Tract based spatial statistics in multiple system atrophy: a comparison between clinical subtypes. Parkinsonism Relat Disord. 2014;20:1050-1055.

58. Faber J, Giordano I, Jiang X, Kindler C, Spottke A, Acosta-Cabronero J, et al. Prominent White Matter Involvement in Multiple System Atrophy of Cerebellar Type. Mov Disord. 2020;35:816-824.

59. Pang H, Yu Z, Yu H, Li X, Bu S, Liu Y, et al. Advanced Cognitive Patterns in Multiple System Atrophy Compared to Parkinson's Disease: An Individual Diffusion Tensor Imaging Study. Acad Radiol. 2024;10.1016/j.acra.2024.01.006.

60. Shiga K, Yamada K, Yoshikawa K, Mizuno T, Nishimura T, Nakagawa M. Local tissue anisotropy decreases in cerebellopetal fibers and pyramidal tract in multiple system atrophy. J Neurol. 2005;252:589-596.

61. Yang H, Wang X, Liao W, Zhou G, Li L, Ouyang L. Application of diffusion tensor imaging in multiple system atrophy: the involvement of pontine transverse and longitudinal fibers. Int J Neurosci. 2015;125:18-24.

62. Tir M, Delmaire C, le Thuc V, Duhamel A, Destée A, Pruvo JP, et al. Motor-related circuit dysfunction in MSA-P: Usefulness of combined whole-brain imaging analysis. Mov Disord. 2009;24:863-870.

63. Novak P, Williams A, Ravin P, Zurkiya O, Abduljalil A, Novak V. Treatment of multiple system atrophy using intravenous immunoglobulin. BMC Neurol. 2012;12:131.

64. Baudrexel S, Seifried C, Penndorf B, Klein JC, Middendorp M, Steinmetz H, et al. The value of putaminal diffusion imaging versus 18-fluorodeoxyglucose positron emission tomography for the

differential diagnosis of the Parkinson variant of multiple system atrophy. Mov Disord. 2014;29:380-387.

65. Meijer FJ, van Rumund A, Tuladhar AM, Aerts MB, Titulaer I, Esselink RA, et al. Conventional 3T brain MRI and diffusion tensor imaging in the diagnostic workup of early stage parkinsonism. Neuroradiology. 2015;57:655-669.

66. Huppertz HJ, Möller L, Südmeyer M, Hilker R, Hattingen E, Egger K, et al. Differentiation of neurodegenerative parkinsonian syndromes by volumetric magnetic resonance imaging analysis and support vector machine classification. Mov Disord. 2016;31:1506-1517.

67. Planetta PJ, Ofori E, Pasternak O, Burciu RG, Shukla P, DeSimone JC, et al. Free-water imaging in Parkinson's disease and atypical parkinsonism. Brain. 2016;139:495-508.

68. Krismer F, Seppi K, Göbel G, Steiger R, Zucal I, Boesch S, et al. Morphometric MRI profiles of multiple system atrophy variants and implications for differential diagnosis. Mov Disord. 2019;34:1041-1048.

69. Seki M, Seppi K, Mueller C, Potrusil T, Goebel G, Reiter E, et al. Diagnostic Potential of Multimodal MRI Markers in Atypical Parkinsonian Disorders. J Parkinsons Dis. 2019;9:681-691.

70. Krismer F, Beliveau V, Seppi K, Mueller C, Goebel G, Gizewski ER, et al. Automated Analysis of Diffusion-Weighted Magnetic Resonance Imaging for the Differential Diagnosis of Multiple System Atrophy from Parkinson's Disease. Mov Disord. 2021;36:241-245.

71. Kübler D, Kobylecki C, McDonald KR, Anton-Rodriguez JM, Herholz K, Carter SF, et al. Structural and metabolic correlates of neuropsychological profiles in multiple system atrophy and Parkinson's disease. Parkinsonism Relat Disord. 2023;107:105277.

72. Oba H, Yagishita A, Terada H, Barkovich AJ, Kutomi K, Yamauchi T, et al. New and reliable MRI diagnosis for progressive supranuclear palsy. Neurology. 2005;64:2050-2055.

73. Cosottini M, Ceravolo R, Faggioni L, Lazzarotti G, Michelassi MC, Bonuccelli U, et al. Assessment of midbrain atrophy in patients with progressive supranuclear palsy with routine magnetic resonance imaging. Acta Neurol Scand. 2007;116:37-42.

74. Mangesius S, Krismer F, Gizewski ER, Müller C, Hussl A, Schocke M, et al. 1.5 Versus 3 tesla magnetic resonance planimetry in neurodegenerative parkinsonism. Mov Disord. 2016;31:1925-1927.

75. Andersen AM, Kaalund SS, Marner L, Salvesen L, Pakkenberg B, Olesen MV. Quantitative cellular changes in multiple system atrophy brains. Neuropathol Appl Neurobiol. 2023;49:e12941.

76. Nicoletti G, Rizzo G, Barbagallo G, Tonon C, Condino F, Manners D, et al. Diffusivity of cerebellar hemispheres enables discrimination of cerebellar or parkinsonian multiple system atrophy from progressive supranuclear palsy-Richardson syndrome and Parkinson disease. Radiology. 2013;267:843-850.

77. Blain CR, Barker GJ, Jarosz JM, Coyle NA, Landau S, Brown RG, et al. Measuring brain stem and cerebellar damage in parkinsonian syndromes using diffusion tensor MRI. Neurology. 2006;67:2199-2205.

78. Makino T, Ito S, Kuwabara S. Involvement of pontine transverse and longitudinal fibers in multiple system atrophy: a tractography-based study. J Neurol Sci. 2011;303:61-66.

79. Ito K, Ohtsuka C, Yoshioka K, Maeda T, Yokosawa S, Mori F, et al. Differentiation Between Multiple System Atrophy and Other Spinocerebellar Degenerations Using Diffusion Kurtosis Imaging. Acad Radiol. 2019;26:e333-e339.

80. Krismer F, Seppi K, Wenning GK, Papapetropoulos S, Abler V, Goebel G, et al. Abnormalities on structural MRI associate with faster disease progression in multiple system atrophy. Parkinsonism Relat Disord. 2019;58:23-27.

81. Chung SJ, Cho KH, Lee YH, Yoo HS, Baik K, Jung JH, et al. Diffusion tensor imaging-based pontine damage as a degeneration marker in synucleinopathy. J Neurosci Res. 2021;99:2922-2931.

82. Abos A, Baggio HC, Segura B, Campabadal A, Uribe C, Giraldo DM, et al. Differentiation of multiple system atrophy from Parkinson's disease by structural connectivity derived from probabilistic tractography. Scientific reports. 2019;9:16488.

83. Vemuri P, Castillo AM, Thostenson KB, Ward CP, Raghavan S, Reid RI, et al. Imaging biomarkers for early multiple system atrophy. Parkinsonism Relat Disord. 2022;103:60-68.

84. Nilsson C, Markenroth Bloch K, Brockstedt S, Lätt J, Widner H, Larsson EM. Tracking the neurodegeneration of parkinsonian disorders--a pilot study. Neuroradiology. 2007;49:111-119.

85. Chen B, Fan G, Sun W, Shang X, Shi S, Wang S, et al. Usefulness of diffusion-tensor MRI in the diagnosis of Parkinson variant of multiple system atrophy and Parkinson's disease: a valuable tool to differentiate between them? Clin Radiol. 2017;72:610.e619-610.e615.

86. Ito K, Ohtsuka C, Yoshioka K, Kameda H, Yokosawa S, Sato R, et al. Differential diagnosis of parkinsonism by a combined use of diffusion kurtosis imaging and quantitative susceptibility mapping. Neuroradiology. 2017;59:759-769.

87. Zanigni S, Evangelisti S, Testa C, Manners DN, Calandra-Buonaura G, Guarino M, et al. White matter and cortical changes in atypical parkinsonisms: A multimodal quantitative MR study. Parkinsonism Relat Disord. 2017;39:44-51.

88. Beliveau V, Krismer F, Skalla E, Schocke MM, Gizewski ER, Wenning GK, et al. Characterization and diagnostic potential of diffusion tractography in multiple system atrophy. Parkinsonism Relat Disord. 2021;85:30-36.

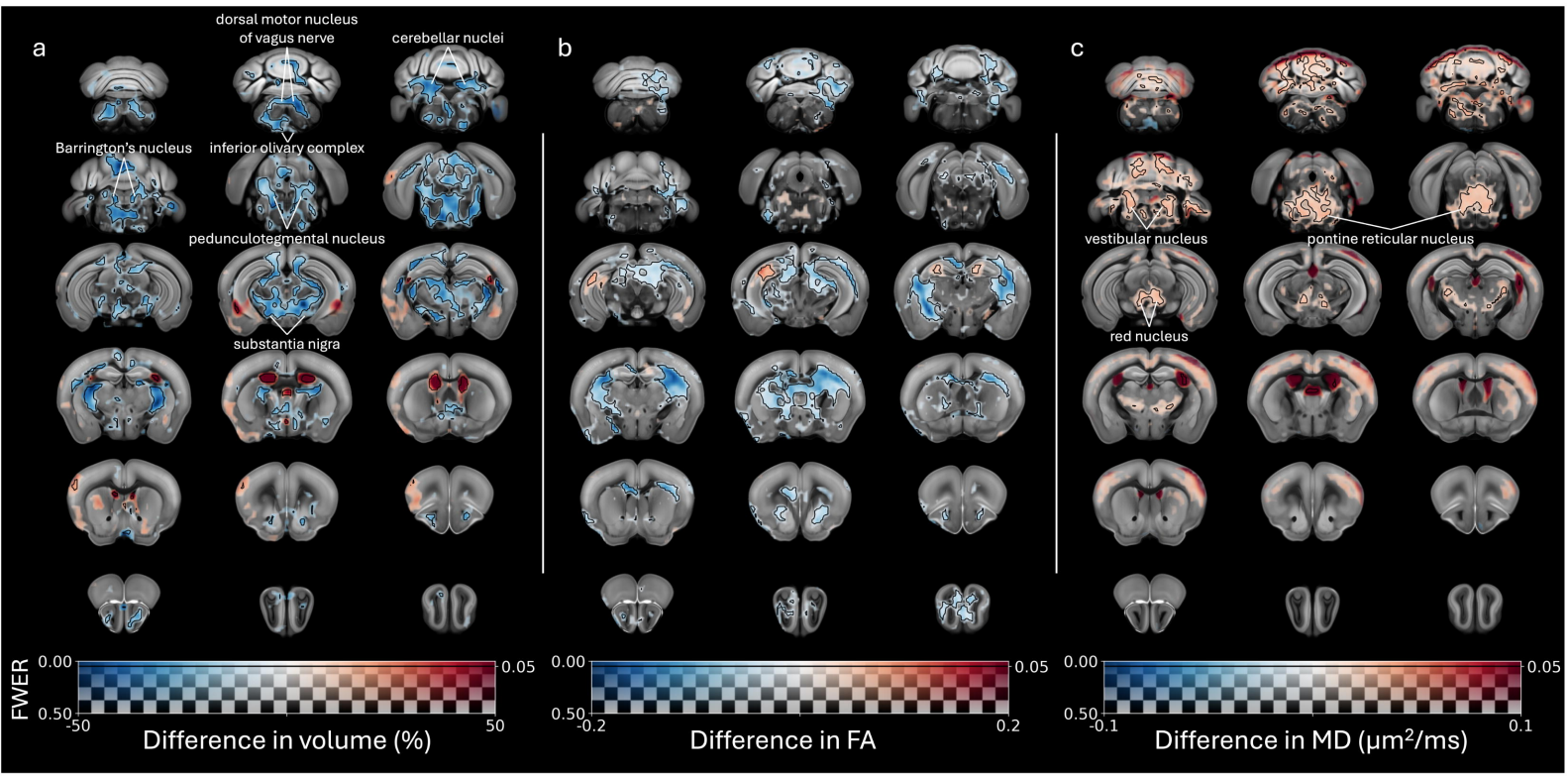

Figure 1. Multi-parametric MRI phenotype of PLP-αSyn brains compared to wild-type mouse brains. Voxel-wise differences in a) volume, b) fractional anisotropy (FA), and c) mean diffusivity (MD) overlaid on the Allen Mouse Brain Common Coordinate Framework (CCFv3) template. The difference in group means (PLP-αSyn minus wild-type) is mapped to the color of the overlays, while the family-wise error rate (FWER) is mapped to the transparency of the overlays. The overlays are completely transparent where the FWER > 0.5, while areas where the FWER < 0.05 are contoured by black lines.

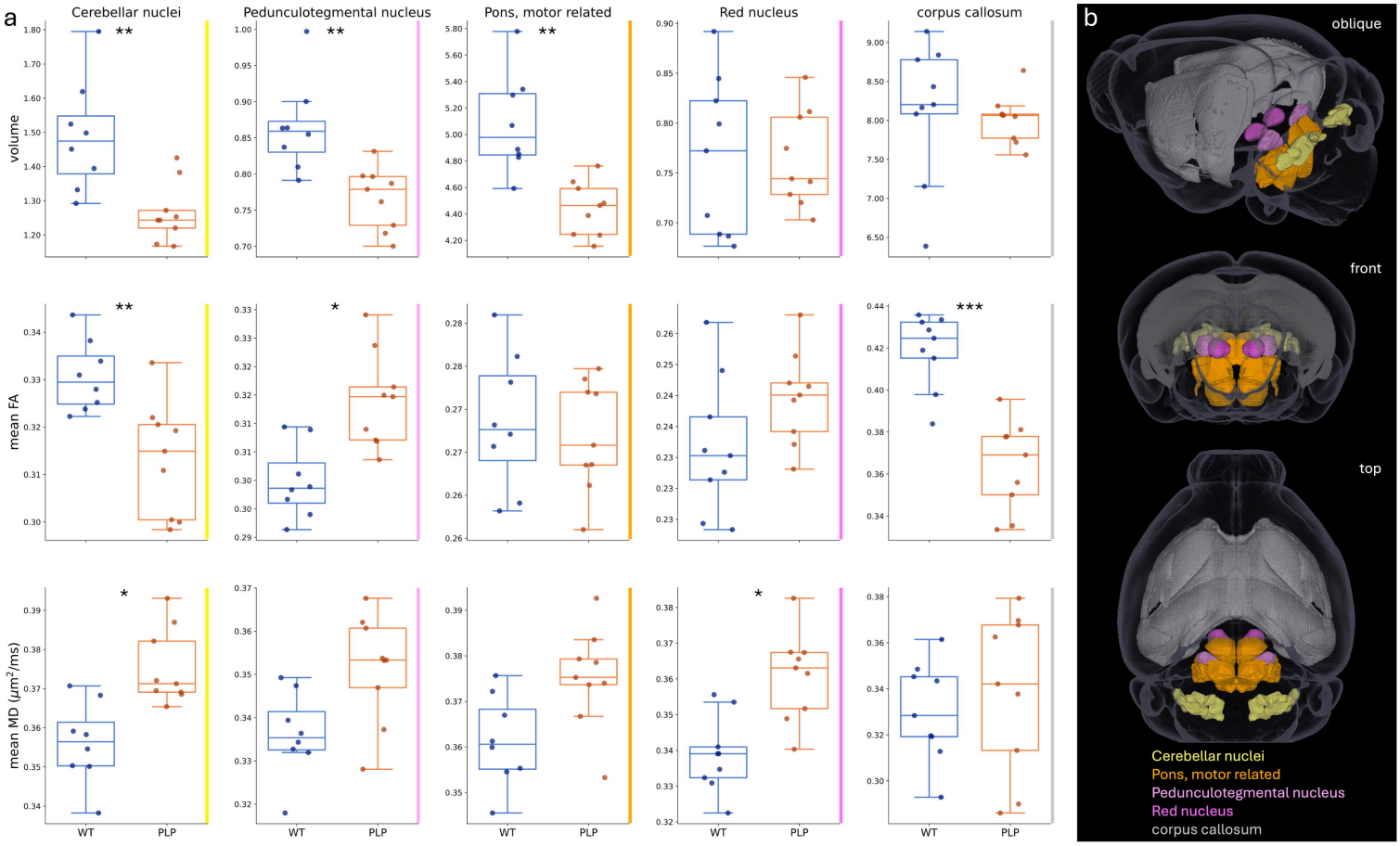

Figure 2. Most affected brain regions in PLP-αSyn mice according to atlas-based statistics of the MRI phenotype. a) Dot and box plots of regional volume, mean fractional anisotropy (FA), and mean mean diffusivity (MD) for select regions-of-interest (ROI). Two-tailed Mann-Whitney U tests, FDR-corrected $p < 0.1$*, 0.01**, 0.001***. b) 3-dimensional representation of the selected ROIs.

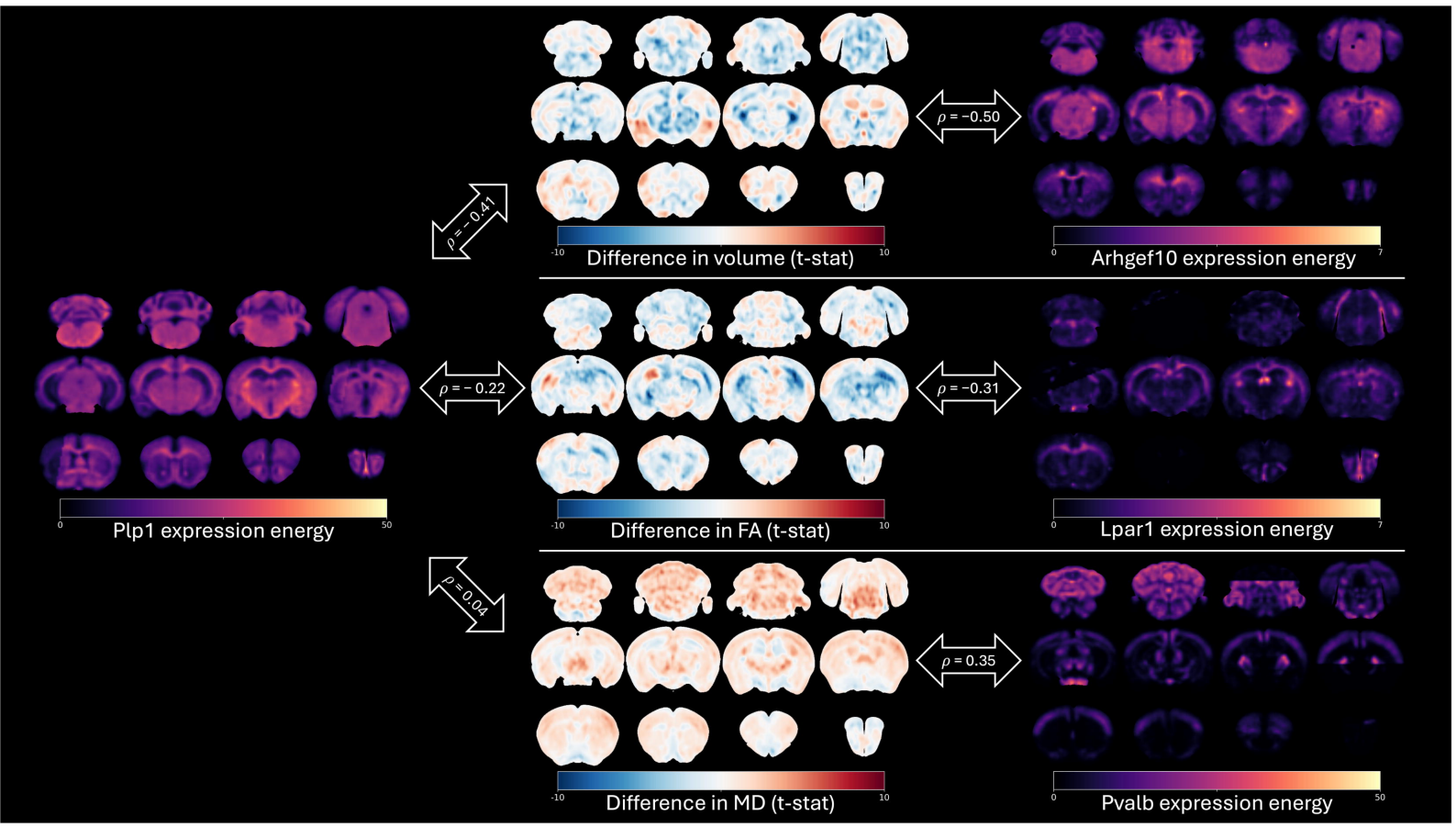

Figure 3. Spatial correlation between the PLP-αSyn MRI phenotype and Allen gene expression maps. Left: coronal slices of the Plp1 expression energy map from the Allen Mouse Brain Atlas. Middle: corresponding slices of t-statistic maps from voxel-wise comparisons of volume, fractional anisotropy (FA), and mean diffusivity (MD) in PLP-αSyn mice vs wild-types. Right: corresponding slices of gene expression energy maps that correlated most strongly with the t-statistic maps. The Spearman correlation coefficients (ρ) between the t-statistic and gene expression maps are shown in the double arrows.

GO terms: Volume-correlated genes

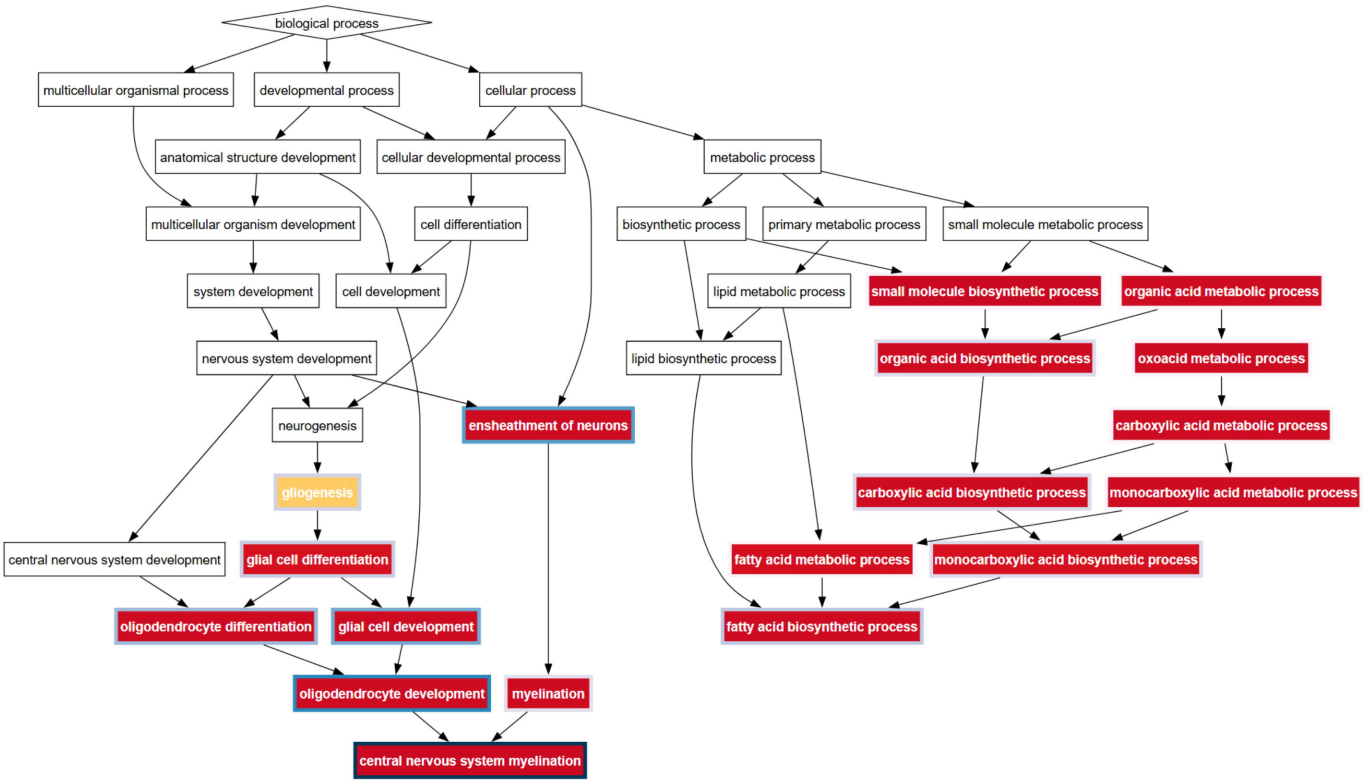

Go terms: FA-correlated genes

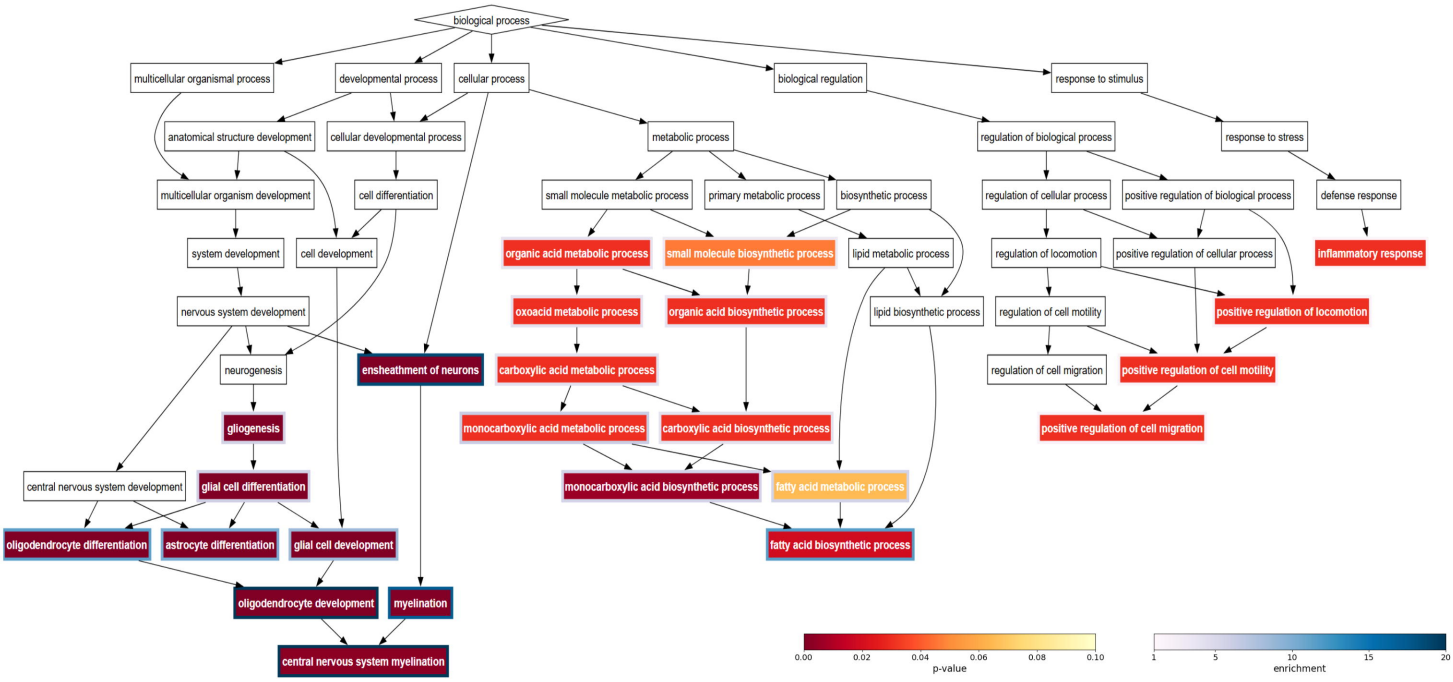

Figure 4. Enriched Gene Ontology terms among genes most spatially correlated with the PLP-αSyn MRI phenotype. Directed acyclic graphs of Gene Ontology (GO) biological process terms containing Plp1 that are significantly enriched (Benjamini-Hochberg-corrected $p < 0.05$) in the top of ranked lists of genes most correlated with PLP-αSyn changes in a) volume and b) fractional anisotropy (FA). For readability purposes, parent terms were included in the graph only if they are in the shortest path between a significantly enriched term and the root "biological process" term. The GO term nodes are colored if corrected $p < 0.1$, with the node outline color indicating the enrichment score. For a given GO term, enrichment = (b/n) / (B/N), where N is the total number of genes in the ranked list; B is the number of genes associated with the GO term; n is the size of the target set, i.e., the number of genes in the top of the ranked list that gives the minimum hypergeometric (mHG) score; and b is the number of genes in the target set that are associated with the GO term.

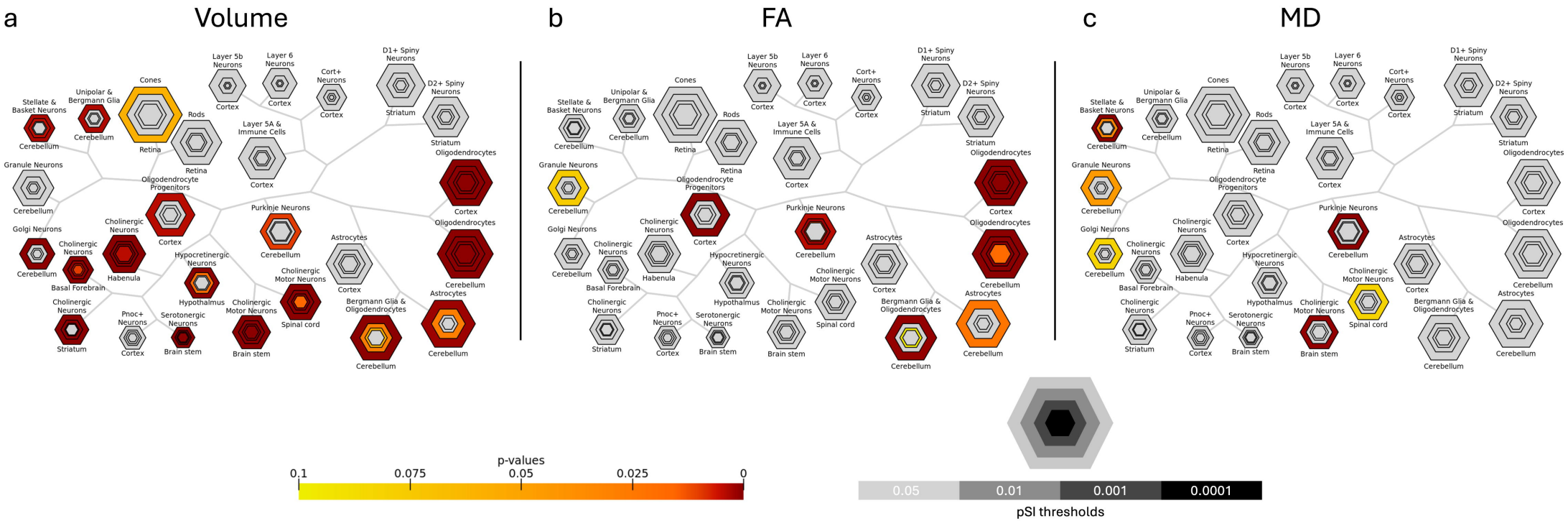

Figure 5. Enriched cell types in genes most spatially correlated with the PLP-αSyn MRI phenotype. Each cell type is represented by four concentric hexagons, the areas of which are proportional to the number of gene that are enriched in that cell type at four different Specificity Index (pSI) thresholds. The smallest, central hexagon represents the list of genes that are most specifically enriched in a particular cell type. The hexagons are grouped by brain region, indicated by the background color. Hexagons are colored if there is an enrichment (Benjamini-Hochberg-corrected $p < 0.1$) of genes associated with the corresponding cell-type in the ranked lists of genes most correlated with PLP-αSyn changes in a) volume, b) fractional anisotropy (FA), and c) mean diffusivity (MD).

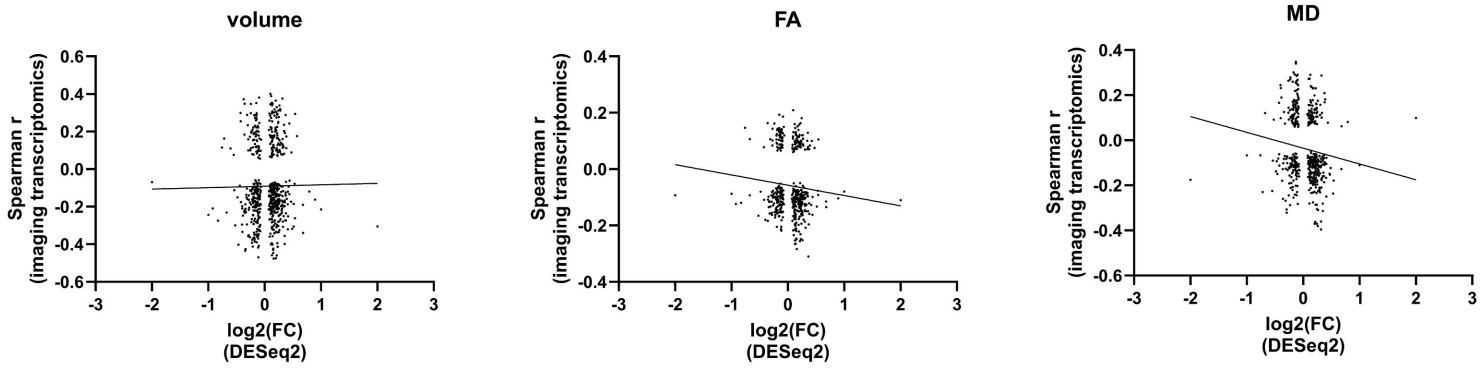

Figure 6. Spearman correlation analysis of DEGs in the cerebellum and MRI–linked genes identified by imaging transcriptomics. The Spearman correlation coefficients between genes' normative spatial expression patterns (Allen Mouse Brain Atlas) and MRI-measured volume, fractional anisotropy (FA), and mean diffusivity (MD) changes in the PLP-αSyn brain are plotted against the genes' log2(FC) from DESeq2 analysis of PLP-αSyn cerebellar tissue.